WPEDU-PR(18) 19259

O Grover et al.

Limit cycle oscillations and Reynolds stress measurements with Langmuir and ball-pen probes on COMPASS

Preprint of Paper to be submitted for publication in
Nuclear Fusion

This work has been carried out within the framework of the EUROfusion Consortium and has received funding from the Euratom research and training programme 2014-2018 under grant agreement No 633053. The views and opinions expressed herein do not necessarily reflect those of the European Commission.

Limit cycle oscillations and Reynolds stress measurements with Langmuir and ball-pen probes on COMPASS

O Grover[1,2], J Seidl[1], D Refy[3], J Adamek[1], P Vondracek[1,4], M Tomes[1,4], P Junek[1], P Hacek[1,4], J Krbec [1,2], V Weinzettl[1], M Hron[1], S Zoletnik[3] and the COMPASS team[1]

[1]Institute of Plasma Physics of the Czech Academy of Sciences, Prague, Czech Republic

[2]Faculty of Nuclear Sciences and Physical Engineering, Czech Technical University in Prague, Czech Republic

[3]Wigner RCP, Budapest, Hungary

[4]Faculty of Mathematics and Physics, Charles University, Prague, Czech Republic

E-mail: grover@ipp.cas.cz

Abstract. This contribution presents the experimentally observed edge plasma evolution during limit cycle oscillations (LCO) measured with a new Langmuir and ball-pen multi-pin probe head at the COMPASS tokamak. The observed LCO regime modulates the intensity of density fluctuations δn_e, radial electric field E_r and intensity of D_α emission with a frequency 3-5 kHz. The density fluctuations grow after E_r decreases in strength which appears to be strongly correlated with the evolution of the pressure gradient $\partial_r p$, typical of type-J LCO dynamics. The magnetic signature of the LCO shows a left-right asymmetry with propagation from the low to high field side. High-frequency (above 100 kHz) precursor-like oscillations are observed as well.

Keywords: magnetic confinement, tokamak, L-H transition, limit-cycle oscillations, edge-localized modes

Submitted to: *Nucl. Fusion*

1. Introduction

The high confinement mode (H-mode) [1] is a key operating regime for future fusion reactors due to the reduction of turbulent transport in the plasma edge and the consequent improvement in confinement. While the observation of this mode in many devices has resulted in a quite robust description of the edge transport barrier maintained by strong sheared flows responsible for the quenching of turbulent transport [2], a robust model of the dynamical process leading to the emergence of such a barrier is still missing. Such a model is of great interest for predictive modeling of the power

threshold for the so called L-H transition from the L-mode (low confinement) to the H-mode, because designs of future reactors such as ITER and DEMO are currently based on empirical scalings of the threshold with large uncertainties [3].

The phenomenon of limit-cycle oscillations (LCO) a.k.a. the I-phase (intermediary phase) observed on many devices [4] during "gradual" L-H transitions offers an opportunity to study the dynamics of the L-H transition, specifically the interplay between turbulence and sheared flows. The LCO were already predicted by a 0D reduced predator-prey-like model of the L-H transition [5]. In this model and its 1D extensions [6] the turbulence acts as the prey, while the zonal sheared flow [7] with a finite but smaller-than-pressure-gradient radial scale decorrelates the turbulence structures as the predator. The poloidal zonal flow is accelerated by the radial gradient of the perpendicular Reynolds stress (RS) $\langle \tilde{v}_p \tilde{v}_r \rangle$ [8, 9] resulting from the covariance of the poloidal $\tilde{v}_p$ and radial $\tilde{v}_r$ velocities of the turbulent structures. The process was also cast as a transfer of energy between zonal flows and turbulence [10] through the Reynolds power per unit mass $\langle \tilde{v}_p \tilde{v}_r \rangle \partial_r \langle v_p \rangle$ with the velocity shear $\partial_r \langle v_p \rangle$. The energy can be also transported by turbulence spreading, therefore, in experiments with point measurements (not zonally averaged) such as [11] the quantity $\partial_r \langle \tilde{v}_p \tilde{v}_r \rangle \langle v_p \rangle$ including the energy transport is used instead. In the model the zonal flows dissipate in the absence of turbulent drive due to collisional and other damping, thereby locking in a state of oscillation between states of high and low turbulence with the zonal flow intensity lagging by a a phase shift of $\pi/2$ typical of LCO in predator-prey models. Meanwhile, with enough external power input the pressure gradient gradually develops over the low turbulence periods until it results in a mean sheared flow sufficient to decorrelate turbulence continuously.

However, experiments on different devices show differing roles of zonal flows generated by turbulence and the mean sheared flow balanced by the pressure gradient at the plasma edge [12, 4]. On the one hand, there were observations of zonal flows coupled with turbulence in TJ-II [13], axisymetric zonal flows during LCO [14] in DIII-D and geodesic acoustic mode (GAM) activity connected with the L-H transition on ASDEX Upgrade [15] and zonal flow production by turbulent Reynolds stress in Alcator C-Mod [16]. On the other hand, in other experiments on JFT-2M [17] and recently ASDEX Upgrade [18] a negligible role of zonal flows was observed and the role of the mean sheared flow was highlighted. In particular, the observations differ by the time ordering of the radial electric field (absolute intensity) E_r and the turbulence intensity. While in experiments with zonal flow activity the electric field intensity maximum lags the turbulence intensity maximum, the order is reversed in experiments where the electric field is controlled mainly by the pressure gradient. In HL-2A both kinds of evolution were observed [19] with so called type-Y LCO featuring turbulence-generated zonal flows and type-J LCO controlled mainly by the pressure gradient. The type-Y LCO after the L-I transition progresses into the type-J oscillation and an I-H transition is observed only after a type-J oscillation.

Recent analyses of the I-phase on ASDEX Upgrade [20] and EAST [21] also noted

the magnetic signature of the LCO. A likely related phenomenon is the M-mode on JET which also features such a magnetic signature and a periodic modulation of the pedestal profile and the outward flux [22]. In these devices an up-down poloidally asymmetrical magnetic low-frequency oscillation associated with the modulation was observed. Such an up-down asymmetry was theoretically interpreted as the result of ballooning transport on the midplane [23]. In addition to the low frequency magnetic oscillations precursor oscillations were also observed on ASDEX Upgrade, highlighting the similarity between the observed LCO and type-III ELMs.

This study concentrates on oscillation phenomena routinely observed during the L-H (and also H-L) transition in COMPASS discharges. These oscillations have a typical frequency of 3-5 kHz. They can be easily observed on D_α emission as well as on other diagnostics, e.g. magnetic pickup coils, probes, etc. These oscillations were initially thought to be ELMs due to the similarity in D_α emission traces. However, they significantly differ from ELMs routinely observed during ELMy H-mode discharges at least in two main aspects: Their amplitude in D_α emission and the power of magnetic and probe-measured fluctuations is (at least in the initial phases) significantly lower, and they do not reliably follow the frequency scaling with the power through the separatrix reported in Ref. [24]. The latter point was the original reason which brought focus to this phenomena.

For these reasons alternative explanations were sought. One possibility is that these are LCO observed on other devices during the L-H transition. In order to investigate whether these are LCO it was necessary to resolve the temporal interplay between turbulence and flows in the plasma edge. Due to the modest typical edge temperature of $\sim$ 50 eV in the COMPASS tokamak [24] it is possible to directly measure $E \times B$ velocities with probes up to $\sim$ 0.5 mm inside the last closed flux surface (LCFS).

Arrays of Langmuir probes have been already used in HL-2A [19] and EAST [11, 25] for the investigation of LCO. However, such Langmuir probe measurements may be influenced by fluctuations of the electron temperature which may play an important role in fluctuation-based quantities, such as the RS as was shown in [26]. In order to prevent the contamination of measurements by temperature fluctuations and to be able to measure them during the LCO as well, a probe head equipped with both Langmuir (LP) and ball-pen (BPP) [27] probes in similar geometric configurations was developed and used for these experiments. The COMPASS tokamak has also plenty of magnetic Mirnov (pickup) coils for the study of magnetic modes.

The rest of this article is structured as follows: In section 2 the diagnostic and experimental setup is described, in particular the multi-pin probe head design. The results of measurements in a gradual L-I-H transition are reported in section 3.1 and those in a stationary LCO regime in section 3.2. Finally, the article is concluded with key observations and their discussion and future experimental plans in section 4.

2. Methods

2.1. Discharge parameters

All the results presented in this article come from discharges performed in the COMPASS tokamak ($R = 0.56$ m, $a = 0.2$ m) [24]. These were deuterium discharges in a lower single-null diverted configuration with an elongation of 1.78, lower and upper triangularity 0.2 and 0.54 at the LCFS, respectively. The ion ∇B drift direction was in the favourable direction (towards the X-point). The X-point height was quite small in order to prevent contamination of the experiment by modes of a yet-unknown origin with comparable frequencies ($\sim 6-7$ kHz) often observed with a high X-point close to the L-H transition. Chamber conditioning procedures were used, but with no direct Z_{eff} measurement the isotope purity cannot be fully guaranteed. The line-averaged densities were kept in the range of $5-7\cdot10^{19}\,\mathrm{m}^{-3}$ and the toroidal on-axis magnetic field was $B_\phi = 1.15$ T. All the discharges were purely ohmic. In the steady-state oscillation scenario in discharges #13925 and #13926 the plasma current was $I_{pl} \approx 190$ kA. In the current-ramp scenario in discharges #13963 and #13960 the plasma current was ramped up (after shaping) from 200 kA to 250 kA in order to induce a slow L-H transition. Oscillations with similar characteristics such as those reported in this article also often appear in other discharges within a quite wide range of operational parameters. However, the discharges presented in this article constitute the currently best selection in terms of the optimized scenario and simultaneously working diagnostics capable of measuring quantities of interest at the plasma edge with sufficient temporal resolution.

2.2. Probe and other diagnostics

The temporal interplay between turbulence and flows during the oscillations under investigation was measured by ball-pen (BPP) and Langmuir probes (LP) in a special, compact geometric configuration on a horizontally reciprocating probe head on the outer midplane. This configuration enables fast (5 MS/s), simultaneous, multi-point measurements of key quantities such as the floating potential V_{fl}, the plasma potential ϕ, electron temperature T_e, density n (from the ion saturation current I^+_{sat}), poloidal and radial electric fields E_p and E_r. The unique combination of BPPs and LPs enables direct measurement of the plasma potential and the electron temperature (in electronvolts) through the formula $V_{fl} = \phi - \alpha T_e$ where the coefficient α is the logarithm of the ratio of the electron and ion saturated currents and is different for each probe type.

The probe head used in this study is a modification of a similar configuration previously used to investigate the effect of electron temperature fluctuations on the measurement of Reynolds stress with Langmuir and ball-pen probes as reported in Ref. [26]. A detailed description of the original probe head geometry and an assessment of its measurement properties, e.g. the α coefficient of the 2 mm BPPs used, electric field measurement properties, can be found in Ref. [26] as well.

The main differences between the modified and original designs are the addition of probes `BPP4` and `BPP6` in the new modified design and the use of boron nitride (BN) material with greater purity for its construction. The former change enables the calculation of both the electric fields with BPPs at the same virtual point, removing the risk on any phase shift between separated measurement points. The latter change resulted in almost no plasma cooling or perturbation in comparison to the original probe head which significantly cooled the plasma and often led to disruptions as was reported in Ref. [26]. The construction from a BN support in which the probes are directly embedded removed the need for extra shielding, and in conjunction with the triangle-mesh-like placement enables placing probes very close to each other.

Figure 1 shows the schematic of the modified probe head design. The radial separation between the probes is 2.5 mm and the poloidal separation is ~ 4 mm. The radial E_r and poloidal E_p electric fields can be calculated from differences of floating or plasma potentials measured by neighboring LPs or BPPs, respectively. For the datasets presented in this article all the electric fields calculated from differences of plasma potentials of appropriately positioned BPPs were averaged into one virtual point located approximately at the "center of mass" of these BPPs. This procedure should mitigate any effect of a possible time lag between electric fields measured at different positions, which could affect the calculation of the Reynolds stress. `LP1` was set to ion saturated current measurement mode in order to measure density fluctuations. The electron temperature T_e in eV units was calculated from the difference of potentials measured by `BPP5` and `LP3` as $T_e[\mathrm{eV}] \approx (\phi^{\mathrm{BPP5}} - V_{fl}^{\mathrm{LP3}})/2.2$, for details on this method see [27]. The density n (assuming local quasineutrality) was estimated from the ion saturated current under the assumptions of the ion temperature being about double T_e for the sound velocity estimation and using the effective collection area of the probe pin. The probe pin is a graphite cylinder with height 1.5 mm and diameter 0.9 mm. Its effective collection area was assumed to be its rectangular cross section and its top base. The correction proportional to $\sqrt{T_e}$ (from the sound velocity) significantly changes the fluctuation characteristics. Due to the applied assumptions, the density estimate is correct only in terms of the order of magnitude. Finally, the electron pressure p_e was estimated from the product nT_e. The poloidal v_p and radial v_r velocities were obtained as the $E \times B$ velocities calculated from the radial E_r and poloidal E_p electric fields divided by the local toroidal magnetic field B_ϕ (~ 0.9 T around the LCFS in the presented discharges), respectively.

Because this probe head cannot directly measure the radial derivative of the electric field and related quantities (e.g. RS), it is necessary to employ conditional averaging or aggregation of measurements at different radial reciprocation positions for the calculation of higher order radial derivatives. The averaging can be done over the radial reciprocation trajectory within one discharge or over a set of highly repeatable discharges. Due to the limited experimental time and repeatability of discharges the former approach was taken in the presented experiments.

The radial reciprocation trajectories were simple in-out plunges with a velocity

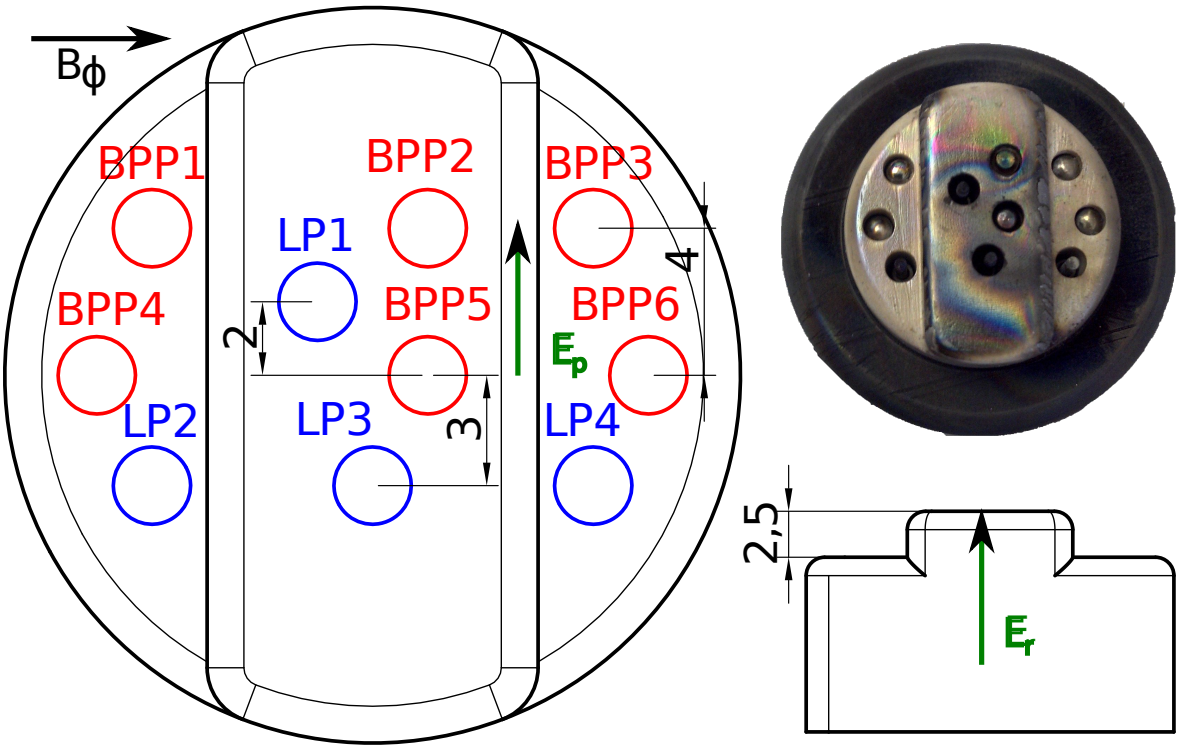

Figure 1. Schematics and a picture of the modfied Reynolds stress probe head containing Langmuir (LP, blue) and ball-pen (BPP, red) probes. All dimensions are in mm. The directions of the toroidal magnetic field B_ϕ, the radial E_r and poloidal electric field E_p are also displayed.

$\sim$ 1 mm/ms, reaching at most $\sim$ 5 mm inside of the LCFS. All radial coordinates in this article are situated on the outer midplane (OMP) and shown with respect to the radial OMP LCFS position. The radial OMP LCFS position obtained from the magnetic reconstruction has a systematic error of $\sim 1-2$ cm as indicated by the associated velocity shear layer (VSL) and the temperature pedestal in diverted plasmas [27, 26]. Fortunately, this systematic offset remains roughly constant during the whole flat-top. For each discharge it was determined as the radial reciprocation position with respect to the magnetic reconstruction LCFS where $\langle E_r \rangle = 0$, i.e. the VSL, and was subtracted before plotting any radial coordinates.

The magnetic signature of the mode associated with the oscillations under study was investigated with two arrays named A and C of magnetic (Mirnov) pickup coils. The arrays are separated by a toroidal angle of $\Delta\phi = 3\pi/4$. Each coil array features 24 coil triplets (measuring all three magnetic field derivative components when connected) approximately uniformly distributed in the poloidal angle [28]. From the A array the coils measuring the components of the magnetic field time derivative locally perpendicular (normal) $\dot{B}_r$ and parallel (tangential) $\dot{B}_\theta$ to the vessel wall were used. From the C array only selected $\dot{B}_\theta$ coils connected to the same data acquisition system were used for the determination of the toroidal mode structure.

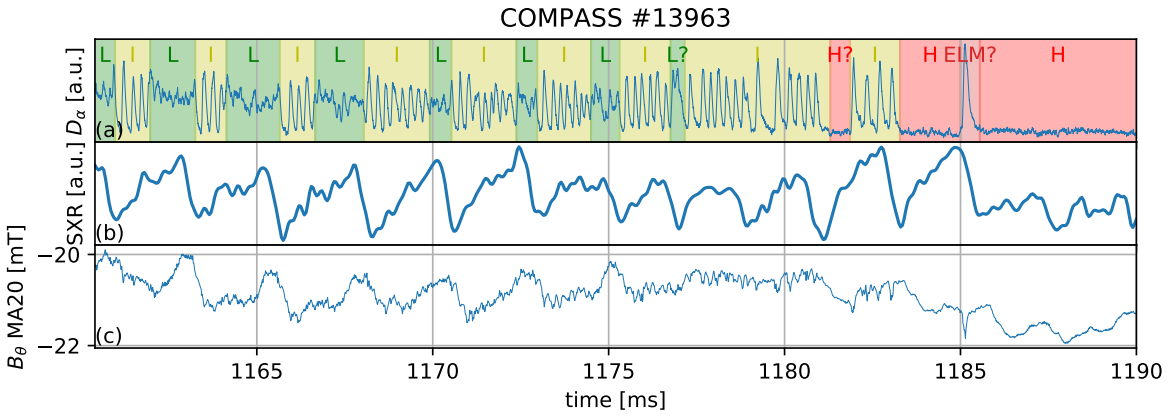

Figure 2. Temporal evolution of selected quantities in the COMPASS discharge #13963, from L-mode through intermittent intermediate phases (I-phase) to the H-mode. The time traces of the (a) D_α emission, (b) core soft X-ray emission, (c) tangential (to vessel) magnetic field measured by Mirnov coil MA20 below the divertor.

The Lithium Beam Emission Spectroscopy (Li-BES) system [29] installed on COMPASS was used to measure density profiles up to the pedestal top in fast chopping mode with 10 μs temporal resolution. Fast chopping mode means that the beam is turned on and off with 100 kHz frequency in order to be able to distinguish between the background and the beam light emission. This is crucial since the LCO modulates the background emission as well.The radial resolution of the system is ~ 1 cm. The system measures profiles approximately on the outer midplane.

3. Results

The gradual L-I-H transition described in the following subsection with intermittent I-phases of several LCOs offers an opportunity to characterize and investigate the L-I transition and the first LCO cycle. The gradual progression from L-mode through I-phases to H-mode was also used to compare the density profiles of these different confinement regimes.

The stationary LCO regime was then used to characterize the LCO cycle with greater temporal and radial resolution in subsection 3.2.

3.1. Slow L-H transition

Figure 2 shows a temporal evolution from L-mode to H-mode through intermittent I-phases with LCO as indicated by the D_α emission intensity in the COMPASS discharge #13963. It is clear that the early L-I transitions as well as later I-H transitions follow the saw-teeth crashes as indicated by the SXR signal from the core. It is not entirely clear whether the later periods of oscillations between prolonged states with an H-mode-like D_α level are still regimes with LCO or small type-III ELMs, because the

typical H-mode confinement time $\sim$ 25 ms in COMPASS is longer than the duration of these phases. The LCO have a distinct signature (negative spikes) in the integrated B_θ signals measured by coil `MA20` below the divertor close to the outer strike-point. These signatures are typically the strongest in the signal from this coil, but other coils at different poloidal locations also measure a clear magnetic signature. The structure of this associated magnetic mode is studied in greater detail in subsection 3.2. Since the D_α evolution is expected to be the result of a complicated process involving SOL transport and wall recycling, the magnetic signature on the coil `MA20` was chosen as the reference LCO phase signal for conditional averaging purposes. The signature of these oscillations in magnetic, D_α and probe measurements becomes stronger as the discharge gradually progresses towards H-mode. There is no clear difference or transition between the early, small oscillations in the L-I-L phases and the oscillations closer to the H-mode which gradually become similar to regular type-III ELMs.

During the observed I-phases close to the L-H transition no significant GAM activity was observed. While some activity in the frequency band 25-35 kHz typical for GAMs on COMPASS as reported in [30] was observed, the activity is very weak in comparison to L-mode levels and only intermittent. The suppression of GAM activity is similar to that observed in H-mode. The GAM appears to recover during the intermittent L-mode phases.

The data measured by the probes in the first three L-I transitions in Figure 2 were conditionally aligned in time according to the instantaneous phase of the B_θ `MA20` signal. The phase was obtained from the analytic signal calculated with the Hilbert transform over a 3.7-5.5 kHz bandpassed version of the signal. This phase-alignment was necessary since the frequency slightly changed throughout the discharge, mostly as a result of density fluctuations. The oscillation frequency appears to be sensitive to density fluctuations during the flat-top. Typically, the LCO frequency decreases with increasing density, but no systematic scaling analysis has been done yet. Since the probe was reciprocating inwards with a speed of $\sim$ 1 mm/ms the measurements were separated by roughly a millimeter. This enables the calculation of approximate radial derivatives from the radially separated measurements conditioned on the MA20 B_θ phase.

The separation of scales into average and fluctuating components was done by time-domain filters as was done in [11]. The separation frequency cutoff was chosen as 13 kHz in order to capture higher harmonics of the base LCO frequency.

The 3 aligned traces of the L-I transitions are shown in Figure 3. The relative time $t_r = 0\,\mu$s corresponds to the π phase of the reference phase signal, i.e. roughly the minimum of the negative spike in the B_θ MA20 signal as can be seen in Figure 3e. The position of the probe during these periods was such that the traces in order correspond to the evolution about 1 mm outside the LCFS, around the LCFS and about 1 mm inside the LCFS.

The saw-tooth crash occurs just before $t_r = -300\,\mu$s and modulates several quantities, e.g. there is a negative spike in the $E_r \times B_\phi$ velocity, and its shear $\partial_r v_p$ is quite high, and the pressure gradient is modulated. The turbulence is gradually

suppressed after $t_r = -250\,\mu$s while the Reynolds stress and its gradient is rather small. This indicates that the initial turbulence suppression is due to the saw-tooth crash changing the core turbulence. During the turbulence suppression period up to $t_r = -150\,\mu$s the pressure gradient inside the LCFS remains relatively high and so does the velocity shear. Outside the LCFS the velocity shear is very low. After this time both quantities decrease inside the LCFS and the turbulence intensity rises as seen in the density fluctuations in the frequency range 250-300 kHz. After $t_r = -100\,\mu$s precursor-like fluctuations at similar frequencies are seen in the magnetic field derivative $\dot{B}_\theta$. The magnetic fluctuations signature appears to be delayed by $\sim 50\,\mu$s with respect to density fluctuations. This may be due to the travel time of the coherent structures from the LCFS midplane to the divertor target. Meanwhile, the pressure gradient inside the LCFS decreases, while it increases outside the LCFS. The fluctuation energy in both E_r and p_e gradually increases. The E_r fluctuations are likely due to coherent structures moving past the probe. During the most turbulent phase the velocity shear remains low and E_r drops to levels outside the LCFS. The Reynolds stress increases during the turbulent phase, but the Reynolds power is very small since the velocity shear is small at that time. Once the turbulence dies away, the velocity shear and the pressure gradient begin to recover.

While the alignment is undoubtedly imperfect and the statistics of only 3 traces is insufficient for straight-forward conclusions, it shows the general ordering of the LCO cycle observed in all the discharges where the probes were measuring.

Figure 4 shows a detailed slice of the density and magnetic fluctuation traces in a typical LCO cycle later in the discharge. The precursor-like density oscillations start at $\sim$ 1177.70 ms in the displayed cycle and typically have a frequency in the range 250-300 kHz. Later they evolve into stronger and more regular fluctuations, typically in the frequency range 100-150 kHz. The magnetic signature also features coherent fluctuations in the 250-300 kHz range, but delayed by $\sim 50\,\mu$s.

The density profiles measured by the Li-BES system in discharge #13960 (similar to #13963 in terms of the gradual L-I-H evolution) conditioned on the phase of the L-I-H transition are shown in Figure 5. The radial coordinate of the density profiles is mapped to the same coordinates as those used with the probe data. However, the VSL position correction comes from the E_r profile measured by the probes. The high/low turbulence intensity conditioning phase of the LCO cycle was obtained as the high/low level of the 2-6 kHz bandpassed envelope of fluctuations in the frequency range 100-250 kHz on an outer Li-BES channel.

The profiles during the phase of high turbulence intensity in the LCO cycle are only marginally steeper deeper inside the LCFS than in the preceding L-mode. However, closer to the LCFS the density is higher than in L-mode and the profile is flattened and extends further into the SOL. The profiles during the phase of low turbulence intensity (quiescent) in the LCO cycle are substantially steeper than in the high turbulence phase, particularly just inside the LCFS. In fact, the largest gradient in the pedestal region is almost as steep as the gradient of the pedestal in the ELM-free H-mode closely after

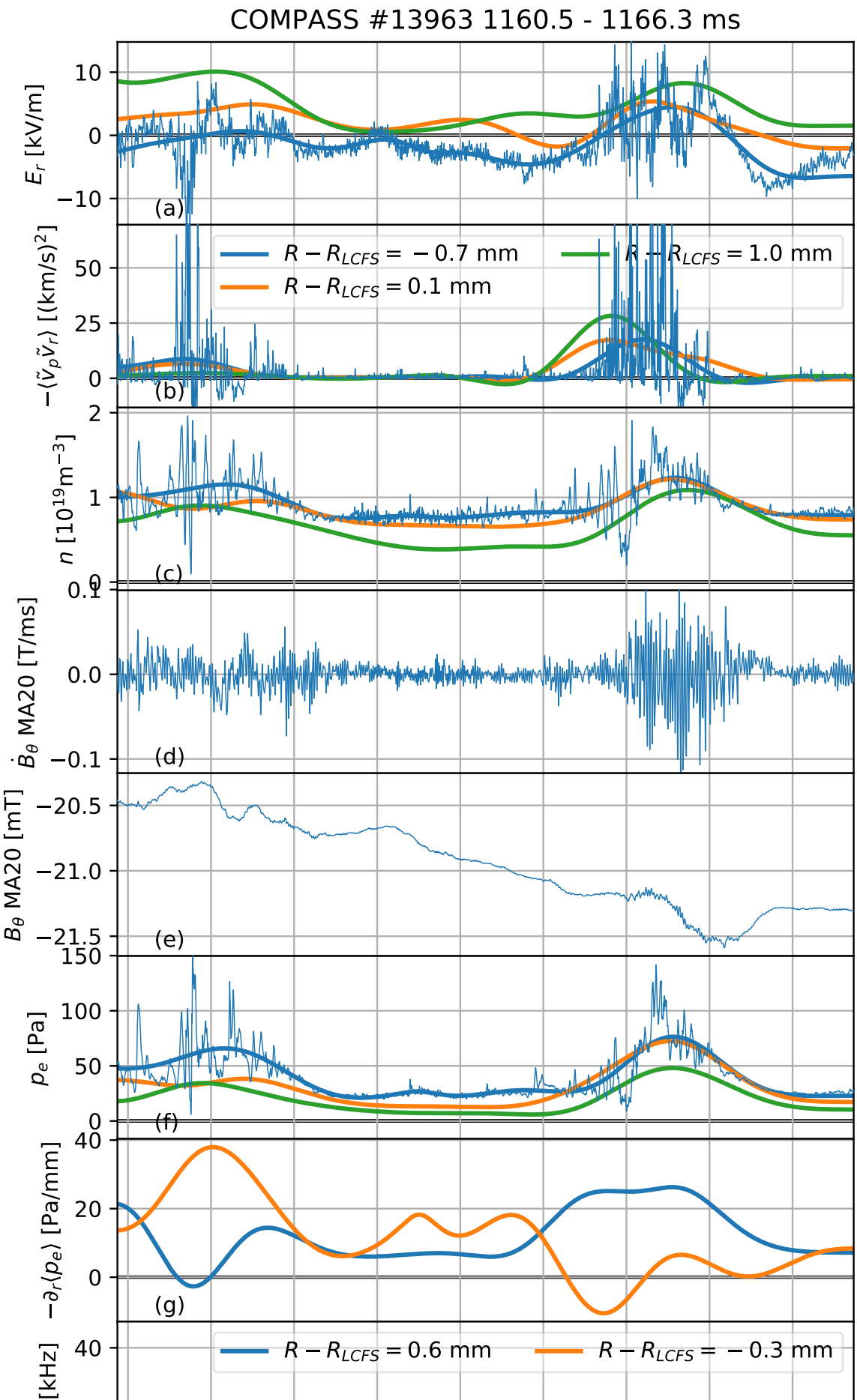
COMPASS #13963 1160.5 - 1166.3 ms
E_r [kV/m]
(a)
$R - R_{LCFS} = -0.7$ mm
$R - R_{LCFS} = 0.1$ mm
$R - R_{LCFS} = 1.0$ mm
$-\langle \tilde{v}_p \tilde{v}_r \rangle$ [(km/s)^2]
(b)
n [10^{19}m^{-3}]
(c)
$\dot{B}_\theta$ MA20 [T/ms]
(d)
B_θ MA20 [mT]
(e)
p_e [Pa]
(f)
$-\partial_r \langle p_e \rangle$ [Pa/mm]
(g)
$R - R_{LCFS} = 0.6$ mm
$R - R_{LCFS} = -0.3$ mm
[kHz]

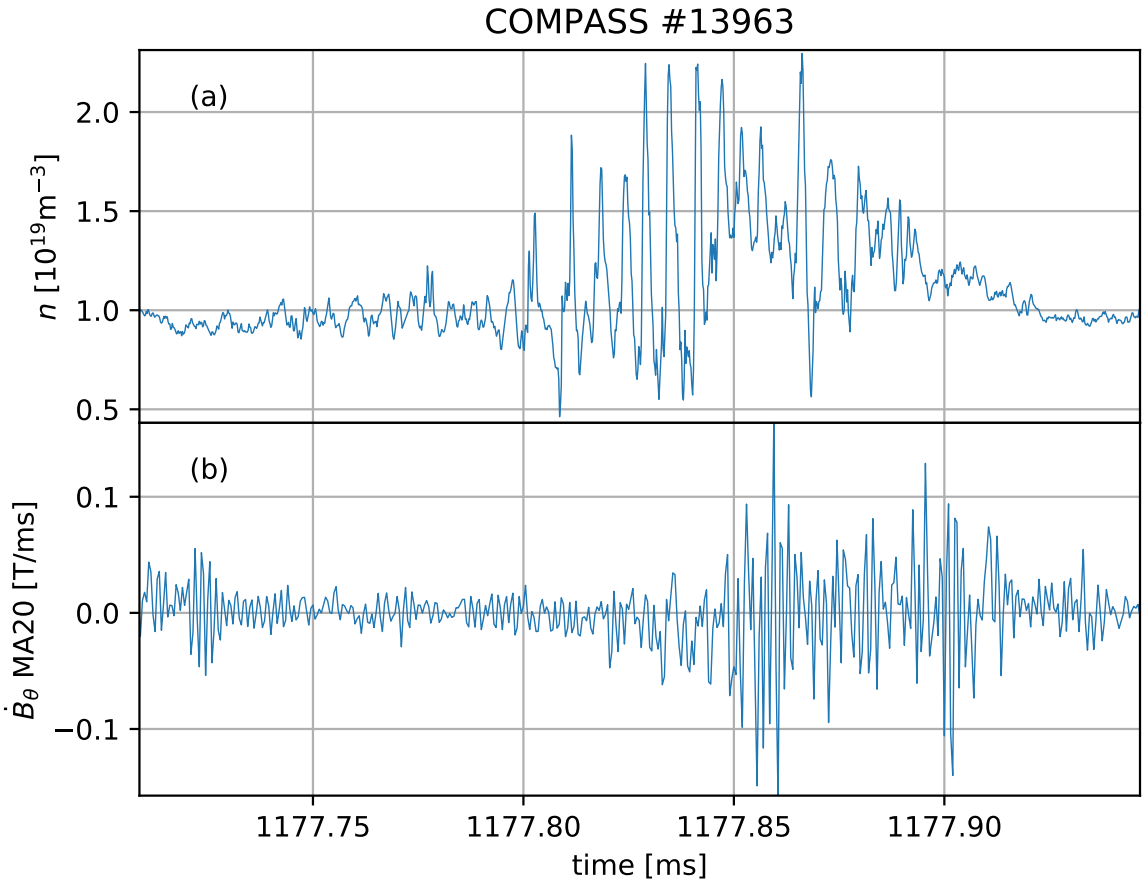

Figure 4. A short segment of the (a) density n and (b) the magnetic field derivative $\dot{B}_\theta$ MA20 traces showing the evolution of the density and magnetic fluctuations during a typical LCO cycle.

the I-H transition. However, the pedestal is much wider in the H-mode profile, resulting in much higher densities deeper inside the LCFS. Altogether, these results suggest that the LCO regime has at least slightly enhanced particle confinement in comparison to L-mode, although it is not at the level of confinement in a fully developed H-mode. The flattening and extension of the profile in the turbulent LCO phase suggests that there is a large flux of particles across the LCFS in this phase.

3.2. Stationary oscillation regime

The discharge scenario with nearly stationary LCO throughout the whole flat-top offers an opportunity to study the LCO evolution with greater radial resolution.

For this purpose the data measured by the reciprocating probe in the range about ±3 mm from the LCFS were conditionally averaged. This average encompassed about 180 LCO cycles. The conditional trigger was again the instantaneous phase of the MA20 B_θ coil signal. The probe data were decimated (lowpassed to Nyquist and downsampled) to a sampling frequency of 1 MHz since no important fluctuations are expected beyond

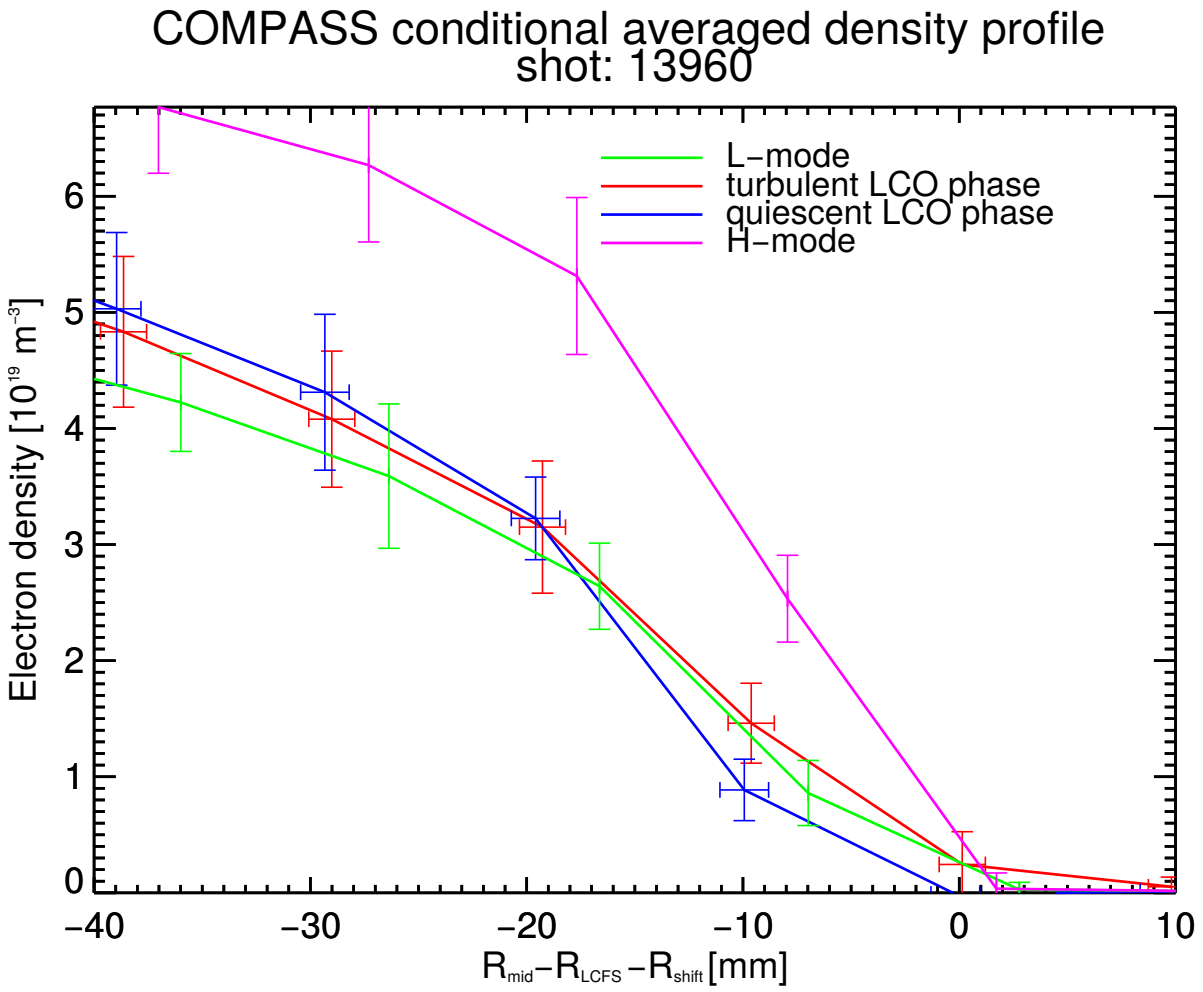

Figure 5. Li-BES density profiles of the edge plasma in the COMPASS discharge #13960. The radial coordinate on the x-axis is the distance from the outer midplane LCFS position with the probe-based VSL correction. Displayed are conditionally averaged profiles in L-mode, LCO phase with high (turbulent) and low (quiescent) turbulence intensity and in H-mode closely after the I-phase. The errorbars represent the standard deviation of the samples in the conditional average.

500 kHz and it reduced the noise in the conditional average. Each data point measured by the probes with a given reciprocation position (again relative to the LCFS up to an offset) and a given MA20 phase was then assigned into a bin in a 2D-histogram-like algorithm which computed the mean and standard deviation of each bin. The resulting 2D map was plotted as contours in Figure 6 for the COMPASS discharge #13926. The result in the discharge #13925 is similar. The radial derivative evolution of plotted quantities can be deduced from the density of contour lines. For better clarity several radial profiles from the same dataset are also plotted in Figure 7. The dashed trends are linear splines with a knot at $R - R_{LCFS} = 0$ mm (except for low density fluctuations where the trend is more complicated). The evolution of means and/or gradients of selected quantities inside and outside the LCFS are plotted as Lissajous curves in Figure 8. Since the LCO frequency was about $\sim$ 4.5 kHz, the conditional

oscillation phase covers about a 220 μs long window.

The conditionally averaged evolution is similar to that described in section 3.1. Starting the description at the point of maximum poloidal velocity (and its shear) inside the LCFS around the $-\frac{1}{4}\pi$ phase of the LCO cycle, the electron pressure profile is the steepest (inside the LCFS) and there is very little turbulence intensity as indicated by the RMS of density fluctuations $\sqrt{\langle\tilde{n}^2\rangle}$. Outside the LCFS the turbulence intensity is also very low, but the velocity shear and the pressure gradient are small. As the oscillation progresses towards $\frac{1}{4}\pi$ the turbulence intensity gradually begins to increase. The turbulence intensity rise is correlated with the rise in the (negative of the) Reynolds stress $-\langle\tilde{v}_p\tilde{v}_r\rangle$ and the radial turbulent transport $\langle\tilde{v}_r\tilde{n}\rangle$. The direction of the average radial turbulent transport is outwards through the LCFS to the SOL. Meanwhile, the pressure profile flattens inside the LCFS and "extends" into the SOL. A similar evolution is visible on the velocity and its shear inside the LCFS. However, outside the LCFS the pressure gradient and the velocity shear slightly increase.

As $\frac{1}{2}\pi$ is approached, the turbulence intensity continues to rapidly increase while the velocity and its shear rapidly decrease inside the LCFS. However, the velocity shear and the pressure gradient slightly increase outside the LCFS.

Once the turbulence intensity and correlated quantities peak around $\frac{1}{2}\pi$ the pressure profile is "ejected" through the LCFS and is generally flattened. The velocity profile is also flattened. The flattening and "ejection" of the pressure profile peaks around the LCO phase $\frac{3}{4}\pi$ while the turbulence intensity is already decreasing.

Afterwards, the pressure profile begins to recover and so does the velocity. It is worth noting that the pressure profile steepness is mostly determined by the temperature profile, the density profile is much flatter inside the LCFS in comparison.

The Reynolds power per unit mass normalized by the effective turbulent energy production $\gamma_{eff}\langle v_\perp^2\rangle$ is negligible throughout the cycle, and reaches only up to $\sim 10\%$ close to the LCFS during the most turbulent phase. The effective turbulence growth rate $\gamma_{eff} \approx 50\,\mu$s was estimated for the average turbulence energy $1/e$ rise time. The apparently negligible role of the Reynolds stress power is mostly due to the velocity (and its shear) inside the LCFS and the Reynolds stress being almost in counter phase.

The Lissajous curves in Figure 8 show that the inside the LCFS the curves of the velocity, its shear and the pressure gradient with respect to the turbulence intensity rotate counter-clockwise, i.e. the velocity and its shear intensity leads the turbulence intensity. It is also interesting to note, that the velocity shear has a more complicated behavior – nearly a a reversal of the curve direction – during the phase of the maximum turbulence intensity which is not so clearly seen on the velocity evolution itself. Outside the LCFS the evolution is reversed in terms of the cycle curve direction with respect to the direction inside the LCFS.

The magnetic signature of the LOC was studied in the discharge #13925 (similar to #13926 but with a more coherent magnetic signature). The evolution of the time derivative of the magnetic field $\dot{B}_\theta$ measured by the Mirnov coil MA20 and also the integrated field B_θ during several LCO periods is shown in Figure 9a,b. The orange curve

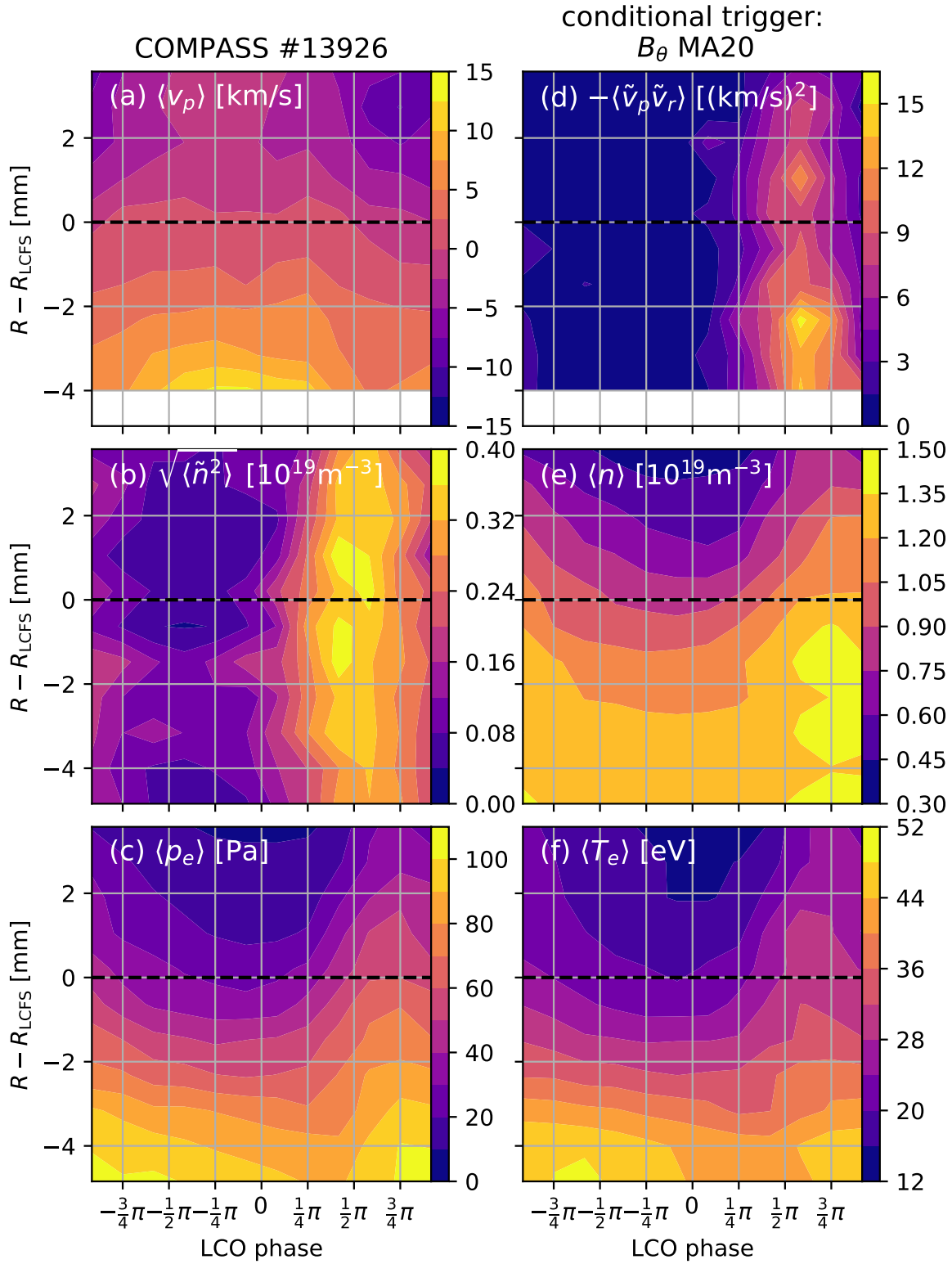

Figure 6. Conditionally averaged evolution of (a) the poloidal velocity $\langle v_p \rangle$, (b) the RMS of density fluctuations $\sqrt{\langle \tilde{n}^2 \rangle}$, (c) the electron pressure $\langle p_e \rangle$, (d) the negative of the Reynolds stress $\langle \tilde{v}_p \tilde{v}_r \rangle$, (e) the density $\langle n \rangle$ and (f) the electron temperature $\langle T_e \rangle$ during an average LCO cycle measured by the Reynolds stress probe head in the discharge #13926.

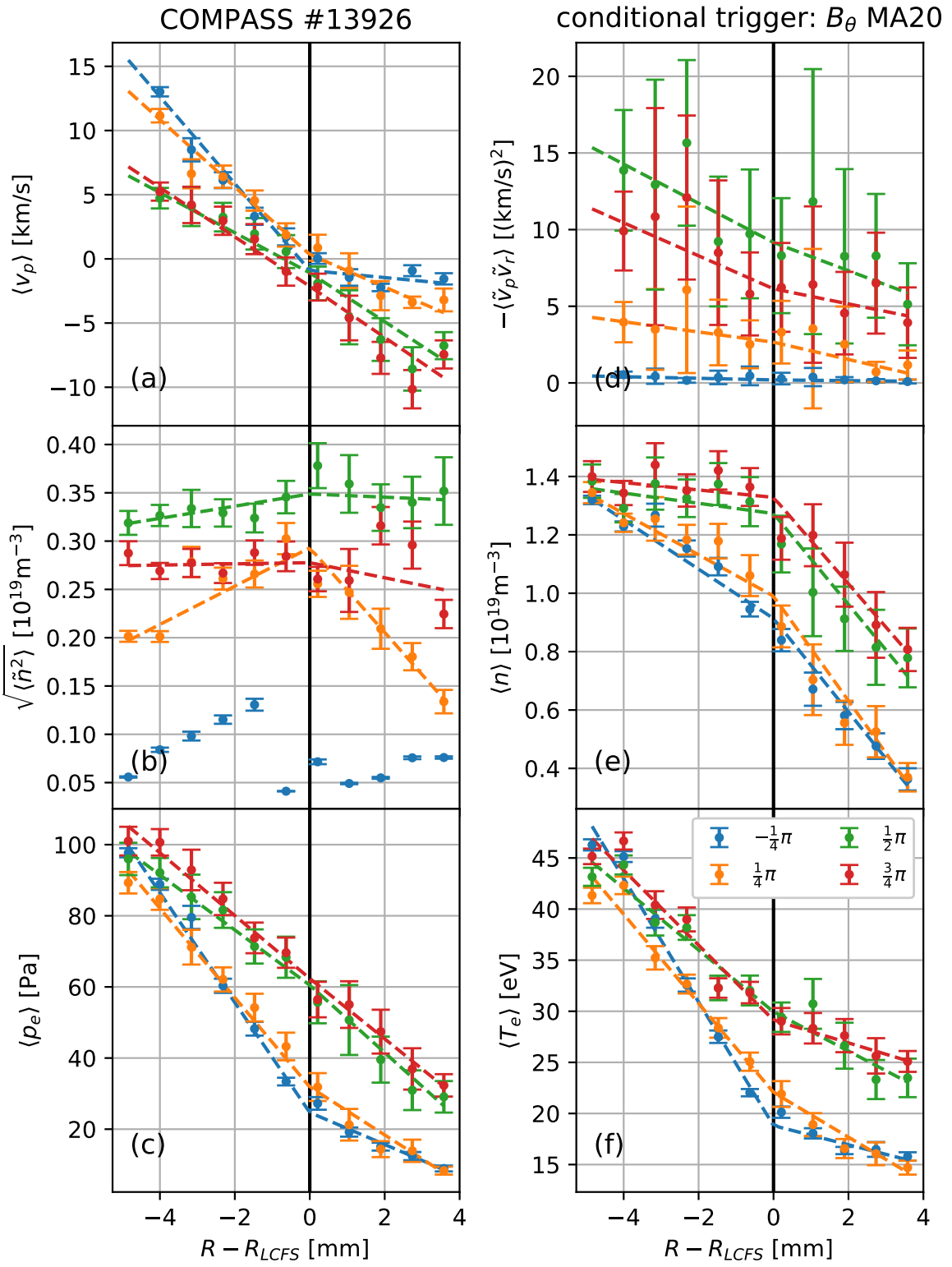

Figure 7. Conditionally averaged radial profiles of (a) the poloidal velocity $\langle v_p \rangle$, (b) the RMS of density fluctuations $\sqrt{\langle \tilde{n}^2 \rangle}$, (c) the electron pressure $\langle p_e \rangle$, (d) the negative of the Reynolds stress $\langle \tilde{v}_p \tilde{v}_r \rangle$, (e) the density $\langle n \rangle$ and (f) the electron temperature $\langle T_e \rangle$ during selected phases of an average LCO cycle measured by the Reynolds stress probe head in the discharge #13926. The dashed trends are linear splines with a knot at $R - R_{LCFS} = 0$ mm.

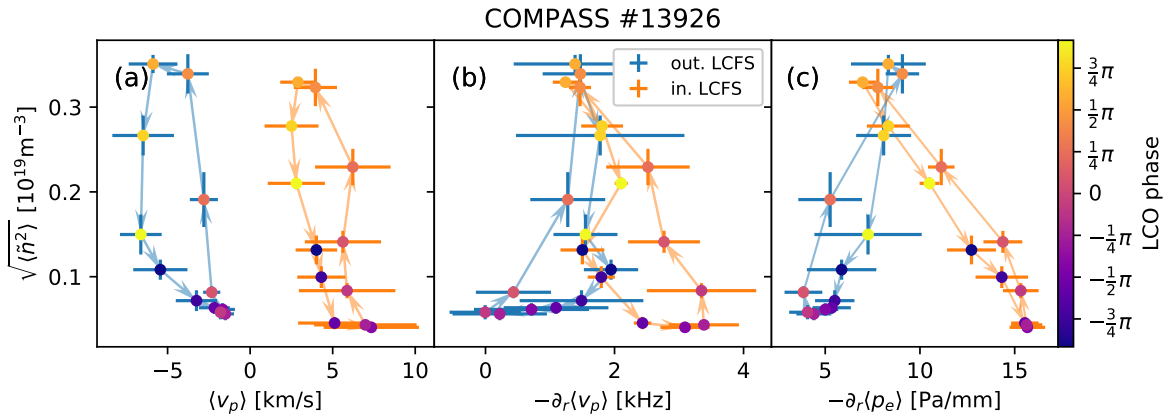

Figure 8. Lissajous curves of conditionally averaged evolution of the RMS of density fluctuations $\sqrt{\langle\tilde{n}^2\rangle}$ of density fluctuations with respect to (a) the the poloidal velocity $\langle v_p\rangle$, (b) the poloidal velocity shear $-\partial_r\langle v_p\rangle$, (c) the negative of the pressure gradient $-\partial_r\langle p_e\rangle$ during an average LCO cycle measured by the Reynolds stress probe head in the discharge #13926. Blue and orange points represent the average and/or gradient of selected quantities inside and outside the LCFS, respectively.

shows the LCO frequency component in the range up to 5 kHz (and from $\sim$ 3.7 kHz in the case of the time derivative). The red curve shows the low-frequency (lowpassed to 20 kHz) envelope of the fluctuation power in the range 20-500 kHz. The fluctuation power is seen to slightly rise (there is a small bump) just before the large burst of fluctuation energy and the large jump in the integrated field. This behavior suggests the presence of precursor-like oscillations.

The cross-coherence of the fields measured by other Mirnov coils in the A array with respect to the the MA20 coil was investigated in 40 ms time window where the LCO frequency was the most stable. The measured $\dot{B}_\theta$ fields exhibit a clear $m, n = 0, 0$ symmetric structure of the envelope of the high-frequency oscillations during the LCOs. The component at the LCO frequency, although weaker, exhibits a left-right asymmetry in the cross-phase as seen in Figure 9c, propagating from the LFS to the HFS. The coherence between coils in the A and C array points to an $n = 0$ mode structure.

The measured B_θ fields at the LCO frequency are systematically stronger than the B_r fields even in the divertor region where the measured mean (equilibrium) fields have strong radial components near the strike points. This suggests that the magnetic activity associated with the LCO is likely located on a closed field line inside the LCFS.

4. Discussion and Conclusions

The oscillation phenomena routinely observed during slow L-H transitions in the COMPASS tokamak was investigated with both ball-pen and Langmuir probes for the first time, offering a direct measurement of the radial electric field without the significant influence of the electron temperature gradient and other fluctuating quantities with high

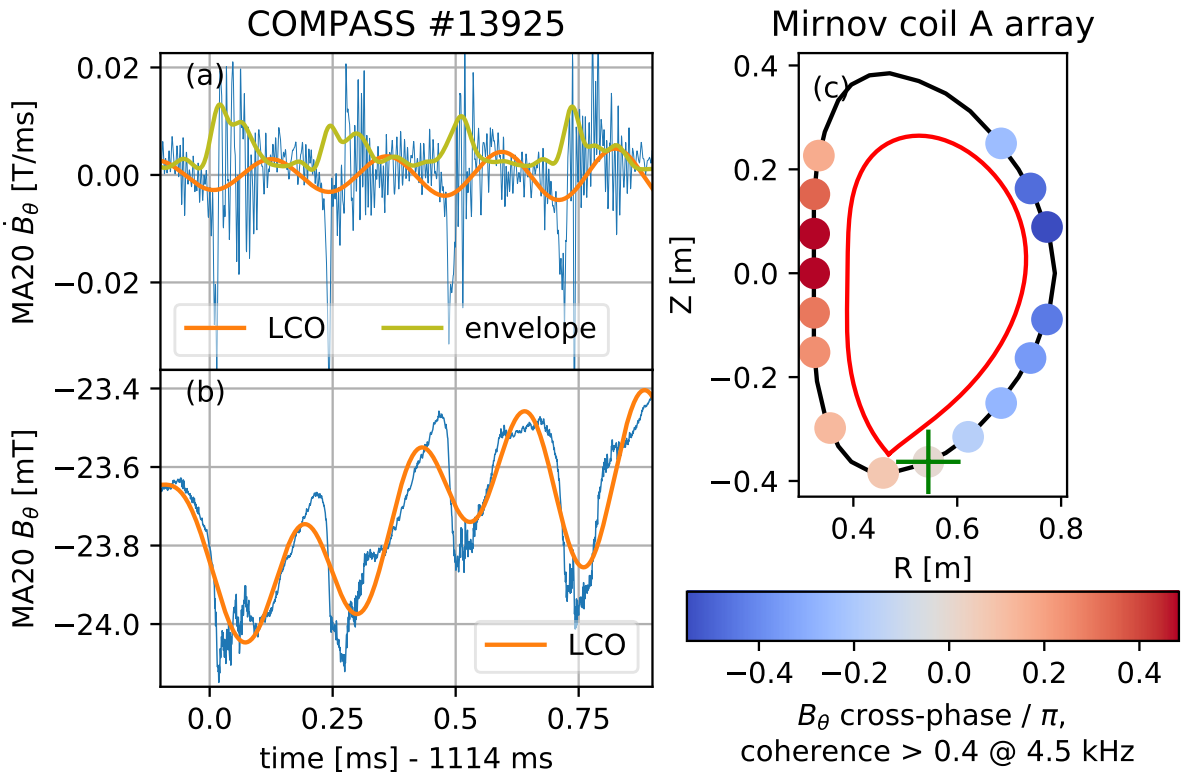

Figure 9. Typical signature of LCO in (a) $\dot{B}_\theta$ and (b) integrated B_θ for the coil MA20. (c) Cross-phase with coherency > 0.4 between fields measured by tangential magnetic pickup coils in array A with respect to the coil MA20 (green cross). The red contour shows the LCFS from the magnetic reconstruction.

temporal resolution.

The temporal ordering of LCO oscillations on COMPASS and the associated radial electric field and the turbulence intensity is consistent with the type-J LCO observed on HL-2A [19]. The apparent lack of Reynolds-stress-related velocity generation and high correlation of the velocity profile with the pressure profile is also consistent with the HL-2A type-J observations. In the state of suppressed turbulence the pressure gradient builds up until some instability leads to its collapse and subsequent ejection of plasma. The turbulence does not recover to L-mode levels, but is suppressed again. The key questions for future studies are which instability triggers the collapse and which mechanism prevents the recovery of L-mode turbulence.

The results also indicate that there may be several different time scales at play, e.g. the fast velocity slow-down, turbulence rise and the profile ejection are faster than the time scale of the gradual pressure and velocity profile recovery and deterioration in the state of low turbulence. The evolution of the shear is also seen to be slightly different from that of the the average velocity. This result suggests that the usage of the poloidal velocity instead of its shear in Ref. [19] may not be completely valid and likely does not show the whole picture.

A significant difference from the HL-2A observations is that the type-J-like

oscillation is observed right after the L-I transition induced by a saw-tooth crash without any preceding type-Y oscillation with significant zonal flow activity as was the case in HL-2A.

However, the presented and fully diagnosed discharges represent only a small set within a larger range of parameters where such oscillations are routinely observed. Therefore, other types of dynamics in different COMPASS scenarios cannot be ruled out. It is also possible that such probe measurements only several mm inside the LCFS do not capture important flow dynamics. This point is supported by the Li-BES density profile showing the largest gradient during the LCO cycle several centimeters inside the LCFS. In a broader sense these results add to the body of experiments where the pressure gradient seems to be the dominant driver of poloidal velocity in LCO and not the zonal flow generated by turbulence.

The magnetic signature observed during the LCO features an asymmetry, but one in the left-to-right direction, whereas on EAST [21], ASDEX Upgrade [20] and the M-mode on JET [22] an up-down asymmetry was observed. The LCO signature in COMPASS appears to be weaker than in ASDEX Upgrade and EAST, but that is likely due to the quite different machine size and correspondingly different density and pressure profiles. The left-right asymmetry should correspond to a pressure gradient modulation according to Ref. [23], which further supports the notion that the LCO is controlled by the pressure gradient.

A more detailed analysis in the future including the localization of the magnetic perturbations on a specific flux surface and possibly the tomographic reconstruction of the corresponding current perturbation could offer more insight.

The presence of precursor-like high-frequency oscillations just before the large LCO-frequency modulation suggests that these oscillations may have some physical mechanisms in common with type-III ELMs. Similar 200-300 kHz precursor-like oscillations are commonly observed in regular type-III ELMs on COMPASS [31] and in ASDEX Upgrade [32]. The larger regular density spikes could be a pre-crash rotating mode such as observed on MAST [33]. Unfortunately, the present measurements do not offer sufficient radial resolution for mode structure and movement analysis. The similarity between these LCO and type-III ELMs was also the general conclusion from ASDEX Upgrade [20].

This similarity with type-III ELMs is further supported by the evolution of the density (and pressure) profiles observed by both probes and Li-BES. A slight pedestal is formed in the LCO regime. The collapse of the gradient during the most turbulent phase of the LCO is followed by a fast "ejection" of the profile into the SOL. The density (and pressure) profile evolution observed by Li-BES and probes qualitatively agree in this regard. The I-phase pedestal appears to be smaller than the one in H-mode, which could explain why the observed LCO have a weaker signature in most signals in comparison to routinely observed type-III ELMs. Therefore, the analysis of profile stability might offer additional insights into the triggering mechanism of the oscillations. However, for such an analysis additional discharges are necessary in order

to obtain a sufficiently large dataset of Thomson scattering pressure profiles. The recent installation of 2 additional lasers [34] will also favor the collection of such a dataset.

While the modified Reynolds stress probe head offers the possibility to directly measure electric fields, it cannot directly measure the radial derivates of these fields and derived quantities of interest (such as the Reynolds stress power). Therefore, a different rake probe head design capable of such measurements is envisioned for future campaigns.

The conditionally-averged Li-BES profile evolution qualitatively agrees with that observed by the probes. However, a more detailed study and comparison of the dynamics observed by both diagnostics is still ongoing and will be the subject of a future publication. It will also focus on the frequency scaling of the LCO, particularly with respect to the edge density measured by the Li-BES system.

The continuing investigation in the COMPASS tokamak and particularly its dependence of this phenomena on various parameters such as the plasma shape, density, proximity to the L-H threshold, etc. is planned as part of the dedicated L-H transition campaign in the first half of the year 2018.

Acknowledgments

We thank Carlos Hidalgo for valuable discussions on the probe head design and Istvan Cziegler for detailed discussions on LCO physics. This work received funding from the Czech Science Foundation projects GA16-25074S and GA15-10723S, MEYS projects 8D15001 and LM2015045 and grant no. SGS15/164/OHK4/2T/14 of the Grant Agency of the Czech Technical University in Prague. This work has been carried out within the framework of the EUROfusion Consortium and has received funding from the Euratom research and training programme 2014-2018 under grant agreement No 633053. The views and opinions expressed herein do not necessarily reflect those of the European Commission.

References

[1] Wagner F, Becker G, Behringer K, Campbell D, Eberhagen A, Engelhardt W, Fussmann G, Gehre O, Gernhardt J, Gierke G v, Haas G, Huang M, Karger F, Keilhacker M, Klüber O, Kornherr M, Lackner K, Lisitano G, Lister G G, Mayer H M, Meisel D, Müller E R, Murmann H, Niedermeyer H, Poschenrieder W, Rapp H, Röhr H, Schneider F, Siller G, Speth E, Stäbler A, Steuer K H, Venus G, Vollmer O and Yü Z 1982 *Phys. Rev. Lett.* **49**(19) 1408–1412

[2] Wagner F 2007 *Plasma Physics and Controlled Fusion* **49** B1 URL `http://stacks.iop.org/0741-3335/49/i=12B/a=S01`

[3] Ikeda K 2007 *Nuclear Fusion* **47** URL `http://stacks.iop.org/0029-5515/47/i=6/a=E01`

[4] ITOH K, ITOH S I and FUJISAWA A 2013 *Plasma and Fusion Research* **8** 1102168–1102168

[5] Kim E J and Diamond P H 2003 *Phys. Rev. Lett.* **90**(18) 185006 URL `http://link.aps.org/doi/10.1103/PhysRevLett.90.185006`

[6] Miki K, Diamond P H, Gürcan O D, Tynan G R, Estrada T, Schmitz L and Xu G S 2012 *Physics of Plasmas* **19** 092306 (*Preprint* `https://doi.org/10.1063/1.4753931`) URL `https://doi.org/10.1063/1.4753931`

[7] Diamond P H, Itoh S I, Itoh K and Hahm T S 2005 *Plasma Physics and Controlled Fusion* **47** R35 URL http://stacks.iop.org/0741-3335/47/i=5/a=R01

[8] Diamond P H and Kim Y B 1991 *Physics of Fluids B: Plasma Physics* **3** 1626–1633

[9] Hidalgo C, Pedrosa M A, Sánchez E, Balbín R, López-Fraguas A, van Milligen B, Silva C, Fernandes H, Varandas C A F, Riccardi C, Carrozza R, Fontanesi M, Carreras B A and García L 2000 *Plasma Physics and Controlled Fusion* **42** A153 URL http://stacks.iop.org/0741-3335/42/i=5A/a=316

[10] Manz P, Xu M, Fedorczak N, Thakur S C and Tynan G R 2012 *Physics of Plasmas* **19** 012309 (*Preprint* https://doi.org/10.1063/1.3676634) URL https://doi.org/10.1063/1.3676634

[11] Tynan G, Xu M, Diamond P, Boedo J, Cziegler I, Fedorczak N, Manz P, Miki K, Thakur S, Schmitz L, Zeng L, Doyle E, McKee G, Yan Z, Xu G, Wan B, Wang H, Guo H, Dong J, Zhao K, Cheng J, Hong W and Yan L 2013 *Nuclear Fusion* **53** 073053 URL http://stacks.iop.org/0029-5515/53/i=7/a=073053

[12] Schmitz L 2017 *Nuclear Fusion* **57** 025003 URL http://stacks.iop.org/0029-5515/57/i=2/a=025003

[13] Estrada T, Happel T, Hidalgo C, Ascasíbar E and Blanco E 2010 *EPL (Europhysics Letters)* **92** 35001 URL http://stacks.iop.org/0295-5075/92/i=3/a=35001

[14] Schmitz L, Zeng L, Rhodes T L, Hillesheim J C, Doyle E J, Groebner R J, Peebles W A, Burrell K H and Wang G 2012 *Phys. Rev. Lett.* **108**(15) 155002 URL https://link.aps.org/doi/10.1103/PhysRevLett.108.155002

[15] Conway G D, Angioni C, Ryter F, Sauter P and Vicente J (ASDEX Upgrade Team) 2011 *Phys. Rev. Lett.* **106**(6) 065001 URL https://link.aps.org/doi/10.1103/PhysRevLett.106.065001

[16] Cziegler I, Tynan G R, Diamond P H, Hubbard A E, Hughes J W, Irby J and Terry J L 2014 *Plasma Physics and Controlled Fusion* **56** 075013 URL http://stacks.iop.org/0741-3335/56/i=7/a=075013

[17] Kobayashi T, Itoh K, Ido T, Kamiya K, Itoh S I, Miura Y, Nagashima Y, Fujisawa A, Inagaki S, Ida K, Kasuya N and Hoshino K 2014 *Nuclear Fusion* **54** 073017 URL http://stacks.iop.org/0029-5515/54/i=7/a=073017

[18] Cavedon M, Pütterich T, Viezzer E, Birkenmeier G, Happel T, Laggner F M, Manz P, Ryter F, Stroth U and Team T A U 2017 *Nuclear Fusion* **57** 014002 URL http://stacks.iop.org/0029-5515/57/i=1/a=014002

[19] Xu Y, Cheng J, Dong J Q, Dong Y B, Jiang M, Zhong W L, Yan L W, Shi Z B, Huang Z H, Li Y G, Nie L, Xu M, Zhao K J, Ji X Q, Yu D L, Liu Y, Cui Z Y, Chen W, Yang Q W, Ding X T, Duan X R and Liu Y 2015 *Plasma Physics and Controlled Fusion* **57** 014028 URL http://stacks.iop.org/0741-3335/57/i=1/a=014028

[20] Birkenmeier G, Cavedon M, Conway G, Manz P, Stroth U, Fischer R, Fuchert G, Happel T, Laggner F, Maraschek M, Medvedeva A, Nikolaeva V, Prisiazhniuk D, Pütterich T, Ryter F, Shao L, Willensdorfer M, Wolfrum E, Zohm H and the ASDEX Upgrade Team 2016 *Nuclear Fusion* **56** 086009 URL http://stacks.iop.org/0029-5515/56/i=8/a=086009

[21] Xu G, Wang H, Xu M, Wan B, Guo H, Diamond P, Tynan G, Chen R, Yan N, Kong D, Zhao H, Liu A, Lan T, Naulin V, Nielsen A, Rasmussen J J, Miki K, Manz P, Zhang W, Wang L, Shao L, Liu S, Chen L, Ding S, Zhao N, Li Y, Liu Y, Hu G, Wu X and Gong X 2014 *Nuclear Fusion* **54** 103002 URL http://stacks.iop.org/0029-5515/54/i=10/a=103002

[22] Solano E R, Vianello N, Delabie E, Hillesheim J, Buratti P, Réfy D, Balboa I, Boboc A, Coelho R, Sieglin B, Silburn S, Drewelow P, Devaux S, Dodt D, Figueiredo A, Frassinetti L, Marsen S, Meneses L, Maggi C, Morris J, Gerasimov S, Baruzzo M, Stamp M, Grist D, Nunes I, Rimini F, Schmuck S, Lupelli I, Silva C and contributors J 2017 *Nuclear Fusion* **57** 022021 URL http://stacks.iop.org/0029-5515/57/i=2/a=022021

[23] Manz P, Birkenmeier G, Fuchert G, Cavedon M, Conway G D, Maraschek M, Medvedeva A, Mink F, Scott B D, Shao L M, Stroth U and Team A U 2016 *Physics of Plasmas* **23** 052302 (*Preprint* https://doi.org/10.1063/1.4948787) URL https://doi.org/10.1063/1.4948787

[24] Pánek R, Adámek J, Aftanas M, Bílková P, Böhm P, Brochard F, Cahyna P, Cavalier J, Dejarnac R, Dimitrova M, Grover O, Harrison J, Háček P, Havlíček J, Havránek A, Horáček J, Hron M, Imríšek M, Janky F, Kirk A, Komm M, Kovařík K, Krbec J, Kripner L, Markovič T, Mitošinková K, Mlynář J, Naydenkova D, Peterka M, Seidl J, Stöckel J, Štefániková E, Tomeš M, Urban J, Vondráček P, Varavin M, Varju J, Weinzettl V, Zajac J and the COMPASS team 2016 *Plasma Physics and Controlled Fusion* **58** 014015 URL http://stacks.iop.org/0741-3335/58/i=1/a=014015

[25] Xu G S, Wan B N, Wang H Q, Guo H Y, Zhao H L, Liu A D, Naulin V, Diamond P H, Tynan G R, Xu M, Chen R, Jiang M, Liu P, Yan N, Zhang W, Wang L, Liu S C and Ding S Y 2011 *Phys. Rev. Lett.* **107**(12) 125001 URL https://link.aps.org/doi/10.1103/PhysRevLett.107.125001

[26] Grover O, Adamek J, Seidl J, Devitre A, Sos M, Vondracek P, Bilkova P and Hron M 2017 *Review of Scientific Instruments* **88** 063501 (*Preprint* http://dx.doi.org/10.1063/1.4984240) URL http://dx.doi.org/10.1063/1.4984240

[27] Adámek J, Müller H W, Silva C, Schrittwieser R, Ionita C, Mehlmann F, Costea S, Horacek J, Kurzan B, Bilkova P, Böhm P, Aftanas M, Vondracek P, Stöckel J, Panek R, Fernandes H and Figueiredo H 2016 *Review of Scientific Instruments* **87** 043510 URL http://scitation.aip.org/content/aip/journal/rsi/87/4/10.1063/1.4945797

[28] Weinzettl V, Pánek R, Hron M, Stöckel J, Zacek F, Havlicek J, Bilkova P, Naydenkova D, Hacek P, Zajac J, Dejarnac R, Horacek J, Adamek J, Mlynar J, Janky F, Aftanas M, Bohm P, Brotankova J, Sestak D, Duran I, Melich R, Jares D, Ghosh J, Anda G, Veres G, Szappanos A, Zoletnik S, Berta M, Shevchenko V, Scannell R, Walsh M, Müller H, Igochine V, Silva A, Manso M, Gomes R, Popov T, Sarychev D, Kiselov V and Nanobashvili S 2011 *Fusion Engineering and Design* **86** 1227–1231 ISSN 09203796 URL http://linkinghub.elsevier.com/retrieve/pii/S0920379610005594

[29] Anda G, Bencze A, Berta M, Dunai D, Hacek P, Krbec J, Réfy D, Krizsanóczi T, Bató S, Ilkei T, Kiss I, Veres G and Zoletnik S 2016 *Fusion Engineering and Design* **108** 1 – 6 ISSN 0920-3796 URL http://www.sciencedirect.com/science/article/pii/S0920379616303131

[30] Seidl J, Krbec J, Hron M, Adamek J, Hidalgo C, Markovic T, Melnikov A, Stockel J, Weinzettl V, Aftanas M, Bilkova P, Bogar O, Bohm P, Eliseev L, Hacek P, Havlicek J, Horacek J, Imrisek M, Kovarik K, Mitosinkova K, Panek R, Tomes M and Vondracek P 2017 *Nuclear Fusion* **57** 126048 URL http://stacks.iop.org/0029-5515/57/i=12/a=126048

[31] Seidl J, Vanovac B, Adamek J, Horacek J, Dejarnac R, Vondracek P, Hron M and the COMPASS team 2014 Probe measurement of radial and parallel propagation of elm filaments in the sol of the compass tokamak *41st EPS Conference on Plasma Physics* (*europhysics conference abstracts* vol 38F) (European Physical Society) URL http://ocs.ciemat.es/EPS2014PAP/pdf/P5.059.pdf

[32] Mink F, Wolfrum E, Maraschek M, Zohm H, Horváth L, Laggner F M, Manz P, Viezzer E, Stroth U and the ASDEX Upgrade Team 2016 *Plasma Physics and Controlled Fusion* **58** 125013 URL http://stacks.iop.org/0741-3335/58/i=12/a=125013

[33] Kirk A, Dunai D, Dunne M, Huijsmans G, Pamela S, Becoulet M, Harrison J, Hillesheim J, Roach C and Saarelma S 2014 *Nuclear Fusion* **54** 114012 URL http://stacks.iop.org/0029-5515/54/i=11/a=114012

[34] Weinzettl V, Adamek J, Berta M, Bilkova P, Bogar O, Bohm P, Cavalier J, Dejarnac R, Dimitrova M, Ficker O, Fridrich D, Grover O, Hacek P, Havlicek J, Havranek A, Horacek J, Hron M, Imrisek M, Komm M, Kovarik K, Krbec J, Markovic T, Matveeva E, Mitosinkova K, Mlynar J, Naydenkova D, Panek R, Paprok R, Peterka M, Podolnik A, Seidl J, Sos M, Stockel J, Tomes M, Varavin M, Varju J, Vlainic M, Vondracek P, Zajac J, Zacek F, Stano M, Anda G, Dunai D, Krizsanoczi T, Refy D, Zoletnik S, Silva A, Gomes R, Pereira T, Popov T, Sarychev D, Ermak G, Zebrowski J, Jakubowski M, Rabinski M, Malinowski K, Nanobashvili S, Spolaore M, Vianello N, Gauthier E, Gunn J and Devitre A 2017 *Journal of Instrumentation* **12** C12015 URL http://stacks.iop.org/1748-0221/12/i=12/a=C12015